Experimental Visualization of Interstitialcy Diffusion of Li ion in β-Li_2TiO_3

Keisuke Mukai,[1]* Masatomo Yashima,[2]* Keisuke Hibino,[2] and Takayuki Terai[3]

[1] Institute of Advanced Energy, Kyoto University, Kyoto 611-0011, Japan

[2] Department of Chemistry, School of Science, Tokyo Institute of Technology, 2-12-1-W4-17, O-okayama, Meguro-ku, Tokyo, 152-8551, Japan

[3] Department of Nuclear Engineering and Management, School of Engineering, The University of Tokyo, 7-3-1 Hongo, Bunkyo-ku, Tokyo 113-8656, Japan

* Corresponding authors: k-mukai@iae.kyoto-u.ac.jp (KM); yashima@cms.titech.ac.jp (MY).

Supporting Information Placeholder

KEYWORDS: *lithium ion battery, nuclear fusion, diffusion mechanism, neutron diffraction, DFT calculations*

Abstract

Monoclinic lithium metatitanate, β-Li_2TiO_3, is a member of Li_2MO_3 (*M* = Ti, Mn, Sn, Ru, and/or Ir) series and an important cation conductor for various energy applications such as Li-ion batteries and nuclear fusion reactors. Comprehensive knowledge of the crystal structure is vital to understanding the Li-ion diffusion mechanism and several possibilities were proposed previously. However, the exact crystal structure and Li-ion diffusion paths of β-Li_2TiO_3 are still unclear. Here, the results of a neutron diffraction study of high-purity ^{7}Li-enriched β-Li_2TiO_3 is reported. The occupancy factor 0.033(3) and the atomic coordinates of interstitial Li ion in Li–O layer are successfully refined by Rietveld analysis on the time-of-flight neutron diffraction data. The three-dimensional network of Li-ion diffusion pathways is visualized by a combined technique of high-temperature neutron-diffraction and maximum-entropy methods. An interstitialcy diffusion mechanism, in which a lithium ion migrates through both the interstitial tetrahedral and lattice octahedral sites, is proposed for the Li_2MO_3 series.

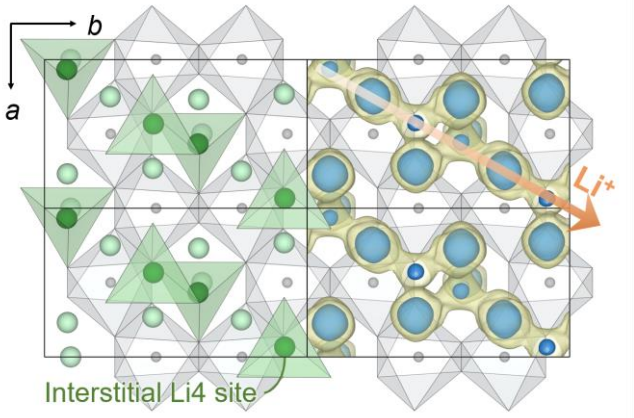

Introduction

Rechargeable Li-ion batteries are key components in portable electronic devices and electric vehicles.[1–3] For large-scale implementation, layered lithium mixed transition-metal oxides, $LiNi_xCo_yMn_{1-x-y}O_2$ materials, where x and y represent Ni and Co contents, have been regarded as alternatives for $LiCoO_2$.[4,5] However, there still remain two major challenges for the use of $LiNi_xCo_yMn_{1-x-y}O_2$, namely (i) enhancement of rate capability to overcome the intrinsically low Li-ion conductivity and (ii) safety issues imposed by the chemical instability of the de-lithiated phase of $Li_{1-z}Ni_xCo_yMn_{1-x-y}O_2$ in organic electrolytes.[6] Li-rich layered oxide Li_2MO_3 (M = Ti/Sn) have attracted significant attention as a coating material for $LiNi_xCo_yMn_{1-x-y}O_2$ cathode in Li-ion batteries, as the coating improves the rate capability as well as the cycling and thermal stability.[7–9] The improved rate capability has been attributed to the three-dimensional (3D) diffusion of Li-ions in Li_2MO_3 (M = Ti/Sn) in contrast to the two-dimensional (2D) diffusion occurring in $LiNi_xCo_yMn_{1-x-y}O_2$.[7–9] Moreover, there has been increasing interest in Li_2MO_3 (M = Ti, Mn, Sn, Ru, and/or Ir) alone as a high-capacity cathode.[10–12]. Thus, understanding the Li-ion diffusion mechanism in Li_2MO_3 (M = Ti, Mn, Sn, Ru, and/or Ir) is highly important to develop better cathode materials for Li-ion batteries. The Li_2MO_3 series commonly has a rock-salt-type structure composed of ordered Li–O and Li–M–O layers along the c-axis. Among the series compounds, as an example material, we herein focus on β-Li_2TiO_3 that has the other important application to use as a ceramic breeder in deuterium-tritium (DT) fusion reactors.[13–15] In the ceramic breeder pebbles of β-Li_2TiO_3, tritium, which is the fuel for DT plasma, is produced by the transmutation of Li ($^6Li + n \rightarrow {}^3T + {}^4He$). The produced tritium migrates to the surface of the pebbles by T^+ bulk and grain-boundary diffusion in β-Li_2TiO_3. T^+ bulk diffusion is important, because it is the rate-determining step for tritium release.[16] Understanding the Li-ion diffusion mechanism is also of particular interest in fusion research as it is closely linked to T^+ bulk diffusion in Li_2TiO_3.[17]

The diffusion of an ionic conductor is strongly dependent on its crystal structure;[18,19] thus, a comprehensive knowledge of the crystal structure of β-Li_2TiO_3 is also required. Single-crystal X-ray and powder neutron diffraction (ND) studies reported that β-Li_2TiO_3 has a monoclinic $C2/c$ structure with an ordered stacking of Li–O and Li–Ti–O layers along the c axis where Li and Ti atoms occupy the octahedral sites (Figure 1c and Figures S1a and S2a in the Supporting Information (SI)).[20–22] In the structure of β-Li_2TiO_3, there exist three Li lattice sites; Li1 and Li2 sites in

the Li–O layer and Li3 site at the centre of the six-membered ring of TiO_6 octahedra in the Li–Ti–O layer (Figure 1c and Figure S2a in SI). In the present investigation, we call this structural model without interstitial Li a 'conventional model' (Figure 1c and Figures S1a and S2a in SI). In addition to the three Li lattice sites, the presence of interstitial Li at the tetrahedral site in the Li–O layer was proposed by using nuclear magnetic resonance (NMR) and molecular dynamics (MD) calculations.[23] Occupation of metal ions at tetrahedral site was reported in $Li_2Ru_{1-y}Ti_yO_3$ as well.[12] However, the interstitial Li atom was not considered in previous structural studies;[20–22] thus, the occupancy factor and atomic coordinates of the interstitial Li ion remain undetermined. One of the aims of this work is to determine the occupancy factor and atomic coordinates of the interstitial Li atom in β-Li_2TiO_3 by the Rietveld analysis of neutron diffraction data. Here, we call the structural model with interstitial Li atoms of β-Li_2TiO_3 an 'interstitial model' (Figures 1d and 1e and Figures S1b and S2b in SI).

The Li-ion diffusion mechanism in β-Li_2TiO_3 is still unclear and a topic of hot debate. Vijayakumar et al.[23] suggested 3D Li-ion diffusion and diffusion pathways through the tetrahedral site along the *c* axis and on the *ab* plane by MD calculations. Similarly, 3D diffusion pathways through a vacant tetrahedral site have been reported for Li_2MnO_3 and Li_2IrO_3 by density functional theory (DFT) calculations.[24,25] On the contrary, using neutron diffraction data, Monchak et al.[26] reported 2D Li-ion diffusion in the Li–O layer and insisted that the Li-ion diffusion along the *c* axis (interlayer diffusion) is less favoured. However, this study has two major problems – (i) large amounts of impurities (Li_2CO_3 and $Li_4Ti_5O_{12}$) in the sample and (ii) noisy neutron scattering length density distribution with ghost peaks. In addition to interlayer diffusion, DFT calculations suggested a different Li-ion diffusion mechanism:[27] straight migration of Li ions between two octahedral Li sites through octahedral interstitial site in the Li–O layer. Due to the structural similarity of monoclinic Li_2MO_3 (*M* = Ti, Mn, Sn, Ru, and/or Ir) materials, revealing Li-ion diffusion mechanism in β-Li_2TiO_3 could have a significant impact on the researches of the series compounds.

To address these unresolved issues, in this report, we conducted a neutron diffraction study using single-phase β-Li_2TiO_3 without impurities. This work employs the maximum-entropy method (MEM), a model-free method originally developed to pick probable information from noisy data.[28,29] MEM is an established and powerful tool to obtain accurate neutron scattering length densities corresponding to given nuclear densities, thus leading to the visualization of ion-diffusion pathways in ionic conductors.[30–32]

Experimental section

Sample preparation

Li_2TiO_3 specimens were prepared by a solid-state reaction route using lithium hydroxide monohydrate ($LiOH·H_2O$, Kojundo Chemical Lab. Co., Ltd.) and metatitanic acid (H_2TiO_3, Mitsuwa Chemicals Co., Ltd.) as the raw materials.[33] A polypropylene bottle containing these powders was rotated on a roller for 24 h at 50 °C. The mixed powder turned into a slurry when a neutralization reaction occurred between the starting materials. The slurry was calcined at 600 °C for 5 h in air atmosphere. The dried powder was molded into pellets at 39 MPa and then sintered at 1200 °C in an Ar atmosphere for 2 h on a dummy pellet of the same composition. The heating rate was 10 K min^{-1}, but cooling was allowed to occur naturally. Using ^{7}Li-enriched $LiOH·H_2O$, $^7Li_2TiO_3$ specimens were fabricated in the same manner for neutron diffraction measurements. The Li/Ti ratio of the synthesized specimens was determined to be 2.00(2) by ICP-AES. No impurity phase was detected by X-ray powder diffraction using Cu $K\alpha$ radiation (RINT-2500, Rigaku).

Neutron diffraction

Time-of-flight neutron diffraction (TOF-ND) measurements of β-Li_2TiO_3 were performed at RT on a versatile neutron powder diffractometer iMATERIA[34] at the MLF of J-PARC of KEK/Japan Atomic Energy Agency (JAEA), Tokai, Japan. The data were analyzed using a Rietveld refinement program, Z-Rietveld,[35] in the range of $0.32 < d < 3.54$ Å. Fixed-wavelength neutron powder diffraction data were collected in air with HERMES[36] at JRR-3 research reactor of JAEA, Tokai. Neutron diffraction data at 27, 400, 600, and 800 °C were conducted with the furnace[37] on a pellet specimen (8.6 mm in diameter, 21.1 mm in height, relative density: 91.1%) in the range of 2θ = 7.0°–156.9° at intervals of 0.1° using a neutron beam with a wavelength of 1.84780(15) Å obtained by a Ge monochromator. Rietveld analyses of the neutron diffraction data of β-Li_2TiO_3 collected by HERMES were performed with RIETAN-FP program.[38] Crystallographic parameters were refined in the REMEDY cycle.[39] Nuclear-density distributions (or more accurately, neutron scattering length density) were obtained by MEM for structure factors obtained from the Rietveld analysis of neutron powder diffraction data collected by HERMES. MEM was performed on a PRIMA program[40] with 100 × 140 × 160 pixels. To estimate the occupancy factor of Li atom, the local integration of the neutron scattering length density at each Li site was carried out based on the Voronoi tessellation using VESTA software.[41]

Ion conductivity

Ion conductivity of β-Li_2TiO_3 was measured by electrochemical impedance spectroscopy on a pellet specimen (11.7 mm in diameter, 7.5 mm in height, relative density: 95.0%). Both sides of the pellet were coated with silver paste and dried for 1 h at 600 °C in Ar. Cathode resistance was measured in air using a three-terminal method with an electrochemical analyzer over a frequency range of 1 MHz to 0.1 Hz without dc bias in the temperature range of 420–500 °C.

Computation

DFT calculations of $(Li_2TiO_3)_{16}$ were performed using the Perdew–Burke–Ernzerhof (PBE)[42] generalized gradient approximation (GGA) for the exchange and correlation functional. Projector augmented wave (PAW) potentials[43] implemented in Vienna *ab initio* simulation package (VASP)[44,45] were used for Li, Ti, and O atoms. 2 × 2 × 2 set of the *k*-point meshes were generated by using the Monkhorst–Pack scheme. A plane-wave cutoff energy of 500 eV was used. Self-consistency was achieved with a tolerance in the total energy of 10^{-5} eV, and the atomic positions were relaxed until the force was less than 0.02 eV $Å^{-1}$. A monoclinic β-Li_2TiO_3 (*C*2/*c*) 2 × 1 × 1 super cell (96 atoms in the perfect crystal) was used for calculations. The nudged elastic band (NEB)[46] method was employed to obtain the minimum energy path for Li-ion migration. In NEB calculations, 7 intermediate images along Li^+ migration paths were optimized in the 2 × 1 × 1 supercell with one negatively charged Li vacancy until the forces were less than 0.03 eV $Å^{-1}$. The NEB calculations for Li^+ migration via vacancy mechanism was performed by removing a Li^+ ion at a lattice site, while the stoichiometric composition including one interstitial Li atom at Li4 site and one Li vacancy at distantly positioned Li3 site was used for simulating Li^+ migration via interstitialcy mechanism. The BVS map for a test Li ion was calculated using the 3DBVSMAPPER program;[47] lattice and positional parameters refined with the TOF-ND data at RT were employed. Using the same program, the BVEL of a test Li ion was calculated with the refined parameters obtained at RT and 800 °C from TOF-ND and fixed-wavelength ND data, respectively. The spatial resolution was set to 0.1 Å. The BVS was calculated using the bond-valence parameters after Brown et al.[48] Possibility of the charge transfer of Li and neighboring Ti atoms during Li-ion migration in β-Li_2TiO_3 was investigated using Bader charge analysis.[49]

Results and Discussion

Crystal structure

^{7}Li-enriched $^{7}Li_2TiO_3$ (^{7}Li > 99.9 wt.%) was prepared to improve the quality of the ND data, as 7.5% ^{6}Li in natural lithium has (i) a neutron absorption coefficient 4 orders of magnitude larger than ^{7}Li, (ii) about 15% lower neutron scattering length, and (iii) causes larger incoherent scattering. Stoichiometric $^{7}Li_2TiO_3$ sample was synthesized by a solid-state reaction method using ^{7}Li-enriched $LiOH{\cdot}H_2O$ and H_2TiO_3.[33] The cation ratio in the Li_2TiO_3 sample was estimated to be Li/Ti = 2.00(2) by inductively coupled plasma atomic emission spectroscopy (ICP-AES), where the number in the parenthesis indicates the standard deviation in the last digit. ND data of $^{7}Li_2TiO_3$ were obtained using a high-resolution time-of-flight (TOF) neutron diffractometer iMATERIA[34] at RT (Figure 1a) and by a constant-wavelength neutron diffractometer HERMES[36] from RT to 800 °C in air (Figure 1b and Figure S3 in SI). X-ray powder diffraction and ND patterns from RT to 800 °C indicated a single phase for monoclinic β-Li_2TiO_3 without impurities, such as Li_2CO_3, $Li_4Ti_5O_{12}$, and high-temperature cubic γ-Li_2TiO_3.

Preliminary Rietveld and MEM analyses of the ND data of $^{7}Li_2TiO_3$ at RT were performed based on the conventional model without interstitial Li atoms (Figure 1c, Figures S1a, S2a, S4a, and 4b, and Tables S1c,d in SI). MEM analysis based on the conventional model indicated a nuclear-density maximum around the tetrahedral vacant site (Wyckoff 8*f* site; atomic coordinates: 0.9,0.1,0.1) in the Li–O layer (dashed circle in Figure S4b of SI), which suggests the existence of interstitial Li atoms. Therefore, we carried out Rietveld and MEM analyses using the interstitial model where the Li atom was placed at the 8*f* site (atom label Li4 in Figures 1d, 1e, 2a, and 2b, Table 1, Figures S1b, S2b, S4c, and S4d in SI, and Tables S1a and S1b in SI). The interstitial model resulted in better (lower) reliability (*R*) factors compared to the conventional model. The *R* factors based on weighted profile intensities, Bragg intensities, and structure factors of the interstitial model (R_{wp} = 10.54%, R_I = 6.88% and R_F = 4.57% (iMATERIA) and R_{wp} = 6.43%, R_I = 1.41%, and R_F = 0.58% (HERMES)) were lower than those of the conventional model (R_{wp} = 10.57%, R_I = 7.05%, and R_F = 4.74% (iMATERIA) and R_{wp} = 6.51%, R_I = 1.65%, and R_F =0.73% (HERMES)). Bond valence sum (BVS) at the interstitial Li4 site was estimated to be 1.16(7), which was consistent with the oxidation number of Li ion (1.00). The bond-valence-based energy landscape (BVEL) of a test Li ion also supported the existence of an interstitial Li4 cation (Figure 2d), which indicates an energy minimum at the Li4 site. The obtained

MEM results were not consistent with the conventional model (Figure S4b in SI), but consistent with the interstitial one (Figure 2b and Figure S4d in SI). At room temperature, the refined occupancy factor of the Li atom at the interstitial Li4 site, 6.6(1.1)% obtained using the HERMES data, agreed with those estimated by the MEM nuclear-analysis (6.3%) (Figures 2b and 3a) and from the iMATERIA data, 3.3(3)%. The presence of an interstitial Li4 atom was also confirmed by DFT structural optimization (Figure 2c) and the calculated formation energies between the interstitial and conventional models were found to be comparable with each other (Table S2 in SI). These results clearly indicate the existence of an interstitial Li4 atom at the tetrahedral site in the Li–O layer of β-Li_2TiO_3.

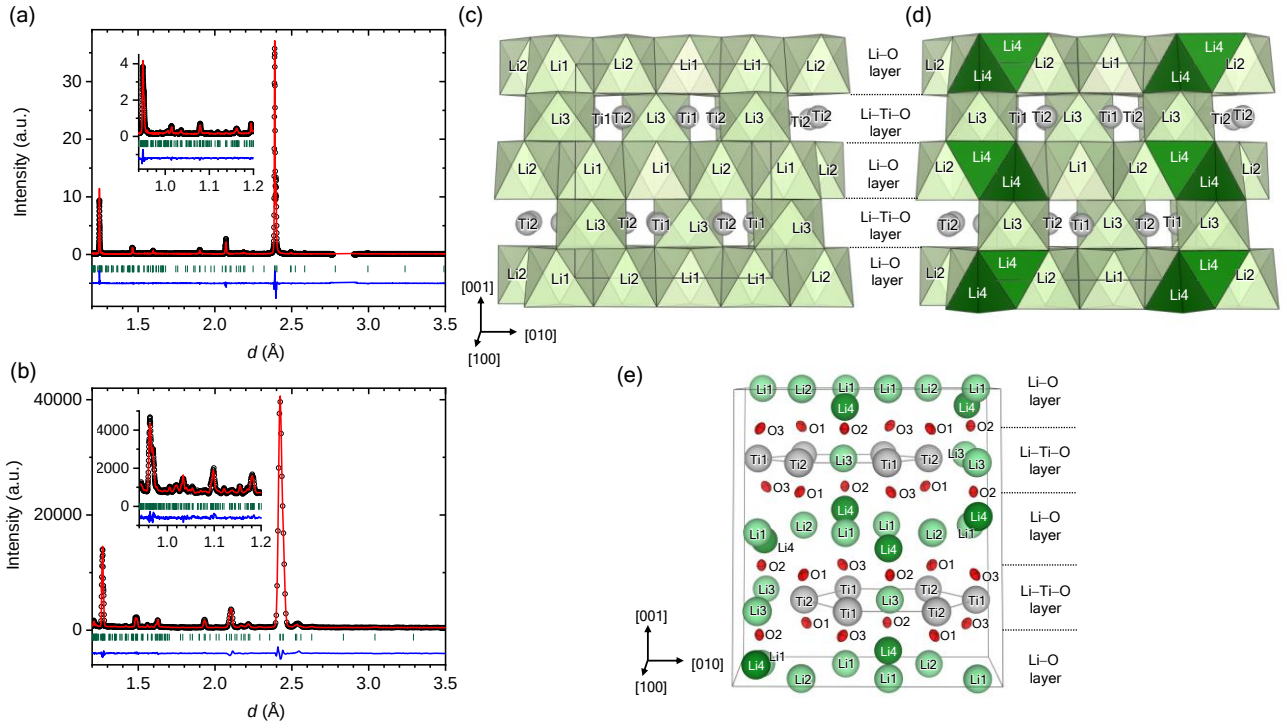

Figure 1. Rietveld patterns of the neutron diffraction data and the refined crystal structure of β-Li_2TiO_3. (a), (b) Rietveld patterns of the neutron-diffraction data measured (a) at RT by the TOF-ND diffractometer iMATERIA and (b) at 800 °C by the fixed-wavelength diffractometer HERMES based on the interstitial model. The black circle, red solid line, blue solid line, and green tick marks in the panels a and b denote the observed intensity Y_{obs}, calculated intensity Y_{calc}, the difference $Y_{calc} - Y_{calc}$, and calculated Bragg peak positions for monoclinic β-Li_2TiO_3, respectively. (c), (d) Refined crystal structures of β-Li_2TiO_3 projected along the [100] direction based on the (c) invalid conventional and (d) valid interstitial models. The light and dark green octahedra and grey spheres represent LiO_6 at Li lattice sites Li*i* (*i* = 1, 2, and 3), $Li4O_4$, and Ti atoms, respectively. **e**, Refined crystal structure of monoclinic Li_2TiO_3 by Rietveld analysis on TOF-ND data at RT with the interstitial model. The light green, dark green, grey spheres and red ellipsoids denote Li at Li*i* lattice sites, interstitial Li at the 8*f* site, Ti, and oxygen ions. Thermal ellipsoids are drawn at the 90% probability level.

Table 1. Refined crystallographic parameters and reliability factors in Rietveld analysis based on the interstitial model using the neutron diffraction data of β-Li_2TiO_3 taken by the iMATERIA at room temperature.

Atom label	Wyckoff site	occupancy	*x*	*y*	*z*	U_{iso}[a] or U_{eq}[b] Å^2	BVS vu
Li1	8*f*	1	0.2435(3)	0.0819(2)	-0.0004(2)	0.0106(3)[a]	0.986(2)
Li2	4*d*	1	1/4	1/4	1/2	0.0098(6)[a]	0.979(1)
Li3	4*e*	0.975(5)	0	0.0908(3)	1/4	0.0076(5)[a]	1.078(2)
Li4	8*f*	0.033(3)	0.933(10)	0.085(6)	0.065(4)	0.0106(3)[a]	1.16(7)
Ti1	4*e*	1	0	0.42621(17)	1/4	0.0040(2)[a]	3.836(5)
Ti2	4*e*	1	0	0.75604(16)	1/4	0.0040(2)[a]	4.105(3)
O1	8*f*	1	0.14271(10)	0.25934(7)	0.13749(7)	0.00529(11)[b]	1.941(7)
O2	8*f*	1	0.10521(10)	0.58551(6)	0.13579(5)	0.00541(10)[b]	2.033(8)
O3	8*f*	1	0.13542(10)	0.90605(6)	0.13542(5)	0.00537(10)[b]	2.048(6)
Space group		*C2/c*					
Lattice parameters		a = 5.066611(16) Å, b = 8.78583(3) Å, c = 9.74892(2) Å, β = 100.1045(3)°, lattice volume: 427.235(3) Å^3					
Reliability factors in Rietveld analysis		R_{wp} = 10.539%, R_p = 7.835%, R_e = 2.565%, R_I = 6.875%, R_F = 4.574%					

[a] U_{iso}: Isotropic ADP of Li*i* and Ti atoms. Linear constraint U_{iso}(Li1) = U_{iso}(Li4) was used in the Rietveld refinement.

[b] U_{eq}: Equivalent isotropic ADP. Refined anisotropic ADPs U_{ij} of oxygen atoms are listed in Table S1a of SI.

Figure 1a and Table 1 show the results of the final refinements of the TOF-ND data of β-$^7Li_2TiO_3$ at RT for the interstitial model. The occupancy factors of the Li atoms at the Li3 and Li4 sites were refined, while those at Li1, Li2, Ti1, Ti2, O1, O2, and O3 sites were fixed to 1. This is because even if these occupancy factors were allowed to vary, the refined occupancy factors were close to 1 within 3 times of the estimated standard deviation and the refinement did not improve significantly. The BVSs of the Li, Ti, and O sites agreed with formal charges of 1.0, 4.0 and 2.0 valence units (vu) (Table 1), which indicates the validity of the refined crystal structure (Figures 1d and 1e; Figures S1b and S2b). The refined atomic coordinates of the interstitial Li4 atom obtained by the Rietveld analysis of the TOF-ND data were (0.933(10), 0.085(6), 0.065(4)), which agreed well with those obtained by DFT structural optimization (0.934, 0.092, 0.071) (Table S2 in SI) and with those where the bond-valence based energy had the minimum value (0.931, 0.089, 0.064) (Figure 2d). These results validate the existence of an interstitial Li ion at the Li4 site. The coordination number of the Li4 atom was 4, which allows the formation of the $Li4O_4$ tetrahedron (Figures 1d and Figure S2b). The refined occupancies at the Li1, Li2, Li3, and Li4 sites (1.00, 1.00, 0.975, 0.033) were consistent with the BVS mismatch | BVS – 1 | values at these sites (0.014, 0.021, 0.078, and 0.16 vu) and with

the bond valence-based energies of a Li ion at these sites (0.01, 0, 0.17, and 0.44 eV). Two Li1, one Li2, one Li3 and four O atoms surround an interstitial Li4 atom (Figure 2a), as predicted computationally.[48] Here, in the case of a Li4 atom, we denote the nearest neighbour Li1 atoms with short and long interatomic distances in the average crystal structure of β-Li_2TiO_3 as Li1 and Li1′, respectively. In the refined average structure of β-Li_2TiO_3 at RT, the Li4–Li*i* interatomic distances, *r*(Li4–Li*i*) [*i* =1, 2, 3], were short: *r*(Li4–Li1) = 1.77(5) Å, *r*(Li4–Li1′) = 1.80(5) Å, *r*(Li4–Li2) = 1.78(5) Å, and *r*(Li4–Li3) = 1.78(4) Å (Figure 2a and Figure S5a in SI). In the DFT optimized structure of $(Li_2TiO_3)_{16}$, the Li1, Li1′, Li2, and Li3 atoms around the Li4 atom were displaced away from Li4 due to Li–Li repulsion (arrows in Figure 2c), resulting in longer Li4–Li*i* interatomic distances of *r*(Li4–Li1) = 2.22 Å, *r*(Li4–Li1′) = 2.21 Å, *r*(Li4–Li2) = 2.22 Å, and *r*(Li4–Li3) = 2.23 Å (Figure 2c and Figure S5b in SI). Therefore, we conclude that β-Li_2TiO_3 with interstitial Li4 is stabilized by the displacement of Li*i* atoms (*i* = 1, 2, and 3) away from the interstitial Li4 atom.

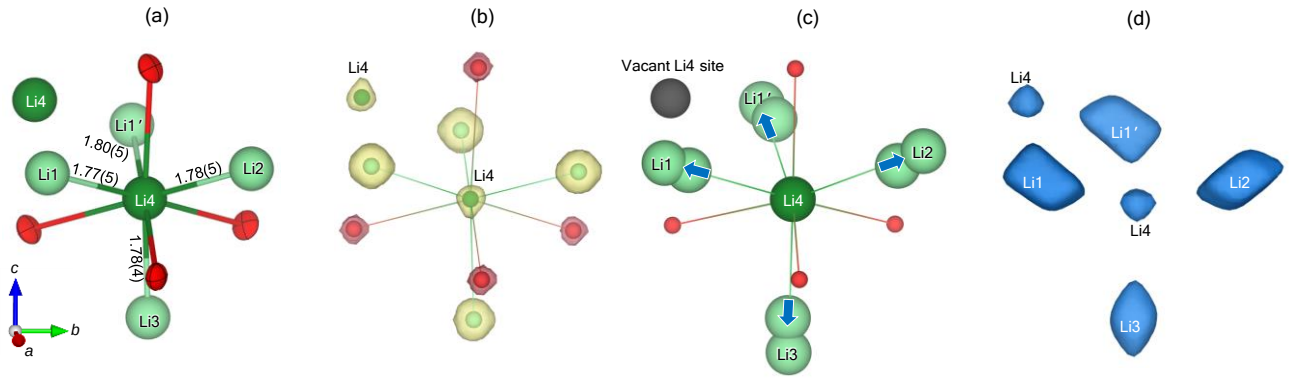

Figure 2. Evidence for the interstitial Li4 cation, and the average and local structures around the Li4 site in β-Li_2TiO_3. (a) A part of the refined structure from the iMATERIA neutron data at RT. In panels (a–c), the light green spheres, dark green spheres, black spheres, and red ellipsoids/spheres denote the Li1, Li1′, Li2, and Li3 atoms at the octahedral sites, interstitial Li4 atom, Li4 site, and oxygen atoms, respectively. The atomic coordinates of the Li4 site are 0.933(10), 0.085(6), and 0.065(4). (b) Isosurfaces of the MEM nuclear densities at 27 °C from the HERMES neutron data where yellow and red surfaces denote the isosurfaces at –1.0 and +1.0 fm $Å^{-3}$, respectively. (c) Local configuration around the interstitial Li4 atom in the structure of $(Li_2TiO_3)_{16}$ optimized by DFT calculations. In panel (c), the blue arrows denote the displacement of Li*i* atoms (*i* = 1, 1′, 2, and 3) in the optimized structure from the positions in the refined average structure. Interatomic distances and atomic positions of Li and O atoms before and after optimization are shown in Figure S5 and Table S3 in SI. The number in panel (a) denotes the interatomic distance with its estimated standard deviation in the parenthesis. The interatomic distances in optimized $(Li_2TiO_3)_{16}$ are shown in Table S1 and Figure S2 in SI. (d) BVEL around the Li4 site with the blue surface at 1.03 eV. In panel (a), thermal ellipsoids are drawn at the 90% probability level. The atomic coordinates at the Li4 site optimized by the DFT calculations agreed well with those refined using iMATERIA neutron data.

ACS Applied Energy Materials DOI: 10.1021/acsaem.9b00639

Diffusion mechanism

ND data of β-$^{7}Li_2TiO_3$ were measured in air at 27, 400, 600 and 800 °C using the HERMES diffractometer and successfully analyzed by the interstitial model (Figure 1b, Figure S3 in SI, and Tables S1b, S4, S5, and S6 in SI). The weight change in Li_2TiO_3 at 800 °C was negligibly small (Figure S6 in SI), which indicates no change in the chemical composition of Li_2TiO_3 during high-temperature ND measurements. Therefore, in Rietveld refinement, we fixed the occupancy factors of Ti and O atoms as 1 and refined the occupancy factors of Li atoms maintaining the atomic ratio of Li/Ti of β-Li_2TiO_3 at 2. The BVSs of Li, Ti, and O sites agreed with formal charges of 1.0, 4.0, and 2.0, respectively, at high temperatures (Figure S7c in SI), which indicates the validity of the refined crystal structures. The refined occupancy factors at high temperatures agreed with the occupancy factors estimated using the MEM nuclear densities (Figure 3a and Figure S8 in SI). These results indicate the validity of the refined crystal structures of β-Li_2TiO_3 from 27 to 800 °C. The lattice parameters *a*, *b*, and *c* and the lattice volume *V* increased with an increase in temperature (Figures S7a in SI), which indicates thermal expansion. The average thermal expansion coefficient along the *c* axis in the temperature range of 27 to 800 °C was 2.344(7) × 10^{-5} K^{-1} and was 1.380(7) and 1.352(7) times higher than those along the *a* and *b* axes, respectively, (Figure S7b), indicating the anisotropic thermal expansion of β-Li_2TiO_3. The average linear thermal expansion coefficient α in the range of 27 to 800 °C was 1.923(4) × 10^{-5} K^{-1}, which is consistent with the reported values of 1.80–2.15 ×10^{-5} K^{-1}.[51,52] The atomic displacement parameters (ADPs) of Li atoms were higher than those of Ti and O atoms (Table 1, Figure 3b). The ADPs of Li atoms increased with temperature, which suggests larger dynamic disorder, positional disorder and thermal motion of Li ions at higher temperatures (Figure 3b). The refined occupancy factor of the Li4 atom increased a little with an increase in temperature, which suggests larger occupational disorder at higher temperatures (Figure 3a). The Li-ion conductivity of β-Li_2TiO_3 increased with an increase in temperature (Figure 3c), which can be attributed to the greater structural disorder and thermal motion of the Li ions at higher temperatures.

ACS Applied Energy Materials DOI: 10.1021/acsaem.9b00639

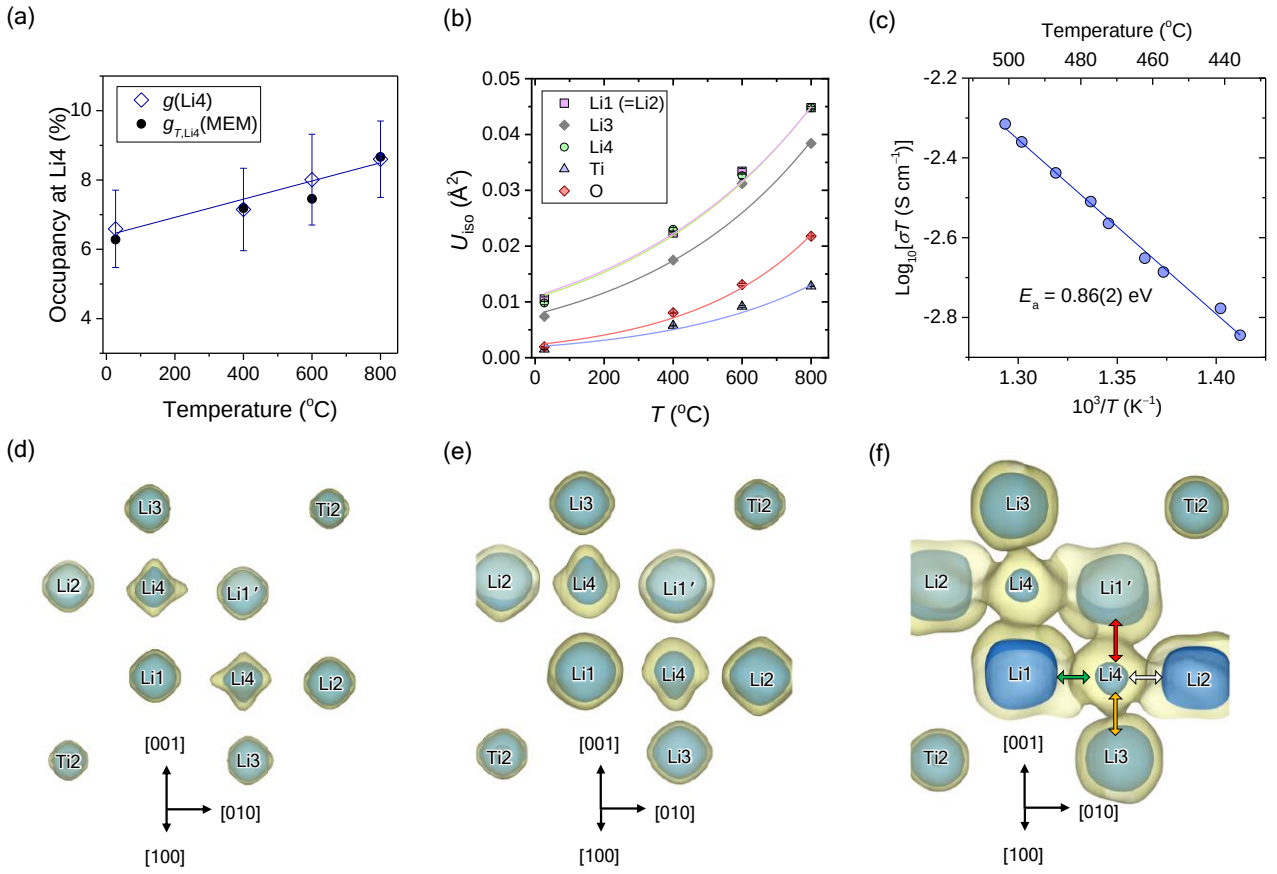

Figure 3. Temperature evolution of the structural disorders and Li-ion conductivity in β-Li_2TiO_3. (a) Refined occupancies at the Li4 site by Rietveld analysis, g(Li4), and the number of Li atoms around the Li4 site $g_{T,MEM}$(Li4) obtained by MEM. $g_{T,Li4}$(MEM) is defined as $g_{T,MEM}(Li4) \equiv g(Li1)I_{T,Li4}/I_{27,Li1}$ where $I_{T,Lii}$ is the integrated value of neutron scattering length density around the Lii site at temperature T (°C). Comparisons at the lattice sites are shown in Figure S8 in SI. The refined occupancies are reliable because of their agreement with the number of atoms around each site obtained by the MEM analysis. (b) Temperature dependence of the refined isotropic atomic displacement parameter (ADP), U_{iso}. (c) Arrhenius plot of Li-ion conductivity σ_{dc}. The activation energy (E_a) for Li-ion diffusion was calculated to be 0.86(2) eV. (d), (e), (f) Yellow and blue isosurfaces of neutron scattering length densities at –0.04 and –0.2 fm Å^{-3}, respectively, at (d) 27, (e) 400, and (f) 800 °C. In panel (f), the red, green, white, and orange arrows denote Li1–Li4, Li1′–Li4, Li2–Li4, and Li3–Li4 Li-ion migration paths, respectively.

The MEM nuclear-density distributions around Li atoms were localized at RT (Figure 3d), while at higher temperatures, the Li atoms exhibited larger spatial distributions (Figures 3e and 3f); this observation is consistent with higher ADPs and Li-ion conductivity at higher temperatures (Figures 3b and 3c). It should be noted that the MEM nuclear-density distributions at 800 °C clearly show connected Li-ion diffusion pathways in the [001], [1$\bar{1}$0], and [110] directions (Figures 4a, 4c, 4e, and 4g). The interlayer [001] pathways across Li–O and Li–Ti–O layers were –Li3–Li4–Li1–Li4–Li3– and –Li3–Li4–Li2–Li4–Li3–; in these, a Li ion migrated from an octahedral Li1 or Li2 site

in the Li–O layer to the octahedral Li3 site in the Li–Ti–O layer via the interstitial Li4 site (Figure 4c). The intralayer [1$\bar{1}$0] pathway in the Li–O layer (–0.1 ≤ z ≤ 0.1) was –Li2–Li4–Li1–Li4–Li2–, where a Li ion migrated from an octahedral Li1 site to another octahedral Li2 position via the interstitial Li4 site (Figure 4e). The intralayer [110] pathway in the Li–O layer (0.4 ≤ z ≤ 0.6) was –Li2–Li4–Li1–Li4–Li2– (Figure 4g). The validity of the [001], [1$\bar{1}$0] and [110] pathways obtained by the MEM analysis at 800 °C was supported by BVEL of a test Li ion (Figure 4b, 4d, 4f, and 4h), BVS maps (Figure S9 in SI) and DFT calculations (Figure S11 in SI). The interlayer [001] pathway consists of –Li3–Li4–Li1– and –Li3–Li4–Li2– paths, while the intralayer [110] and [1$\bar{1}$0] pathways consist of the –Li2–Li4–Li1– path. In all the paths, a Li ion was able to migrate via the interstitial Li4 site, which indicates that the Li4 site is essential for the Li-ion diffusion in β-Li_2TiO_3. It should be noted that the Li ion diffuses via an interstitialcy mechanism in which Li-ion migration occurs through tetrahedral Li4 interstitial site and octahedral Lii lattice sites (i = 1, 2 and 3). The highest nuclear densities on the Li-ion diffusion pathways in β-Li_2TiO_3 at 800 °C were similar, –0.047 fm Å^{-3} for the Li1–Li4 path, –0.052 fm Å^{-3} for Li1′–Li4, –0.047 fm Å^{-3} for Li2–Li4, and –0.046 fm Å^{-3} for Li3–Li4. The bond valence-based energy barriers for Li-ion migration were also similar, 0.91 eV (Li1–Li4), 0.89 eV (Li1′–Li4), 0.97 eV (Li3–Li4), and 0.97 eV (Li3–Li4) at 27 °C and 0.73 eV (Li1–Li4), 0.76 eV (Li1′–Li4), 0.77 eV (Li2–Li4), and 0.76 eV (Li3–Li4) at 800 °C (Figure 4i). These values agree with the experimental activation energy for Li-ion conductivity 0.86 eV (Figure 3c). These results clearly indicate that a Li ion diffuses three-dimensionally via the [001], [1$\bar{1}$0], and [110] pathways. Figure 5a shows Li^+ migration via vacancy mechanism, in which a Li atom at Li1 site migrates through vacant interstitial Li4 site to vacant Li3 site (path I: Li1–Li4–L3) and vacant Li2 site (path II: Li1–Li4–L2). The migration energies for path I and path II were estimated to be 0.52 eV and 0.53 eV (Figure 5c), and those for the paths along Li2–Li4–L3 and Li1′–Li4–Li3 were 0.50 and 0.53 eV (Figure S10 in SI). Li atom can also migrate via interstitialcy mechanism as known as knock-off mechanism where an interstitial Li atom kicks a neighbor Li atom at a lattice Li site out into an adjacent vacant interstitial site (Figure 5b), as reported in Li_2CO_3.[53] The migration energies for path III (B→C, C→V3) and path IV (B→D, D→V4) were estimated to be 0.27 and 0.20 eV, respectively (Figure 5d), indicating the interstitialcy mechanism is energetically favorable. The charge states of migrating Li atoms and neighbor Ti atoms along path III and path IV by Bader analysis suggest that no electron transfer takes place along with Li^+ diffusion (Figure S12 and Table S7 in SI).

ACS Applied Energy Materials DOI: 10.1021/acsaem.9b00639

The MEM results in the current work show the first example of the experimental visualization of 3D Li-ion diffusion pathways through an interstitial Li4 site in β-Li_2TiO_3. Previously, Monchak et al.[26] were not able to detect the interstitial Li4 atom and the [001] Li-ion diffusion path, but reported an invalid zigzag path and 2D Li-ion diffusion on the *ab* plane in MEM nuclear-density distributions from the neutron-diffraction data of a β-Li_2TiO_3 sample at 800 °C. Their sample contained impurities and their results were not consistent with the BVS map. Islam et al. suggested a different Li-ion diffusion mechanism: Li1–Li2 straight migration path for Li ions in the Li–O layer of β-Li_2TiO_3;[27] however, the corresponding path was not observed in the MEM nuclear-density distribution analyzed in this work at 800 °C (Figures S11a and S11b in SI). Our DFT calculations also indicated that the Li1–Li2 straight Li-ion migration path is not energetically favorable due to higher energy barrier of 0.73 eV (Figure S11c in SI) as compared to that for the migration through Li4 site (0.50–0.53 eV) (Figure 5 and Figure S10 in SI).

ACS Applied Energy Materials DOI: 10.1021/acsaem.9b00639

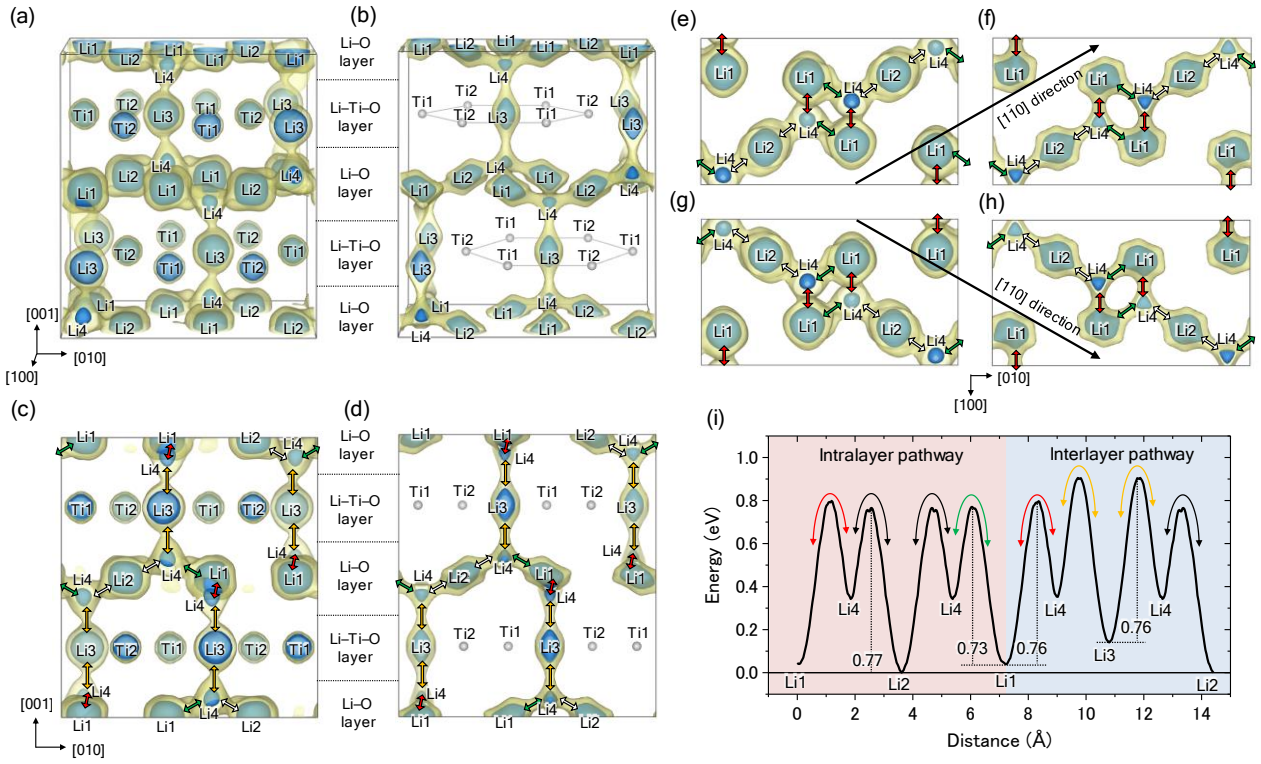

Figure 4. Interstitialcy Diffusion pathways of Li ion in β-Li_2TiO_3 in the <001> and <110> directions. (a), (c), (e), (g), Yellow and blue isosurfaces of neutron scattering length densities of β-Li_2TiO_3 at –0.04 and –0.2 fm $Å^{-3}$, respectively, representing the probability densities of lithium and titanium ions. (b), (d), (f), (h), Yellow and blue isosurfaces of the bond-valence-based energies of a test Li ion at 0.63 and 1.03 eV, respectively, for the refined crystal structure of β-Li_2TiO_3 at 800 °C. **i**, Energy barrier profile of Li ion obtained using the BVEL of β-Li_2TiO_3 at 800 °C. The energy barriers for the Li1–Li4 (green arrows), Li1′–Li4 (red arrows), Li2–Li4 (black arrows), and Li3–Li4 migration paths (yellow arrows) were estimated to be 0.73, 0.76, 0.77, and 0.76 eV, respectively. (a,b) $0 \le x \le 1$, $0 \le y \le 1$, $0 \le z \le 1$. (c,d) $-0.05 \le x \le 0.55$, $0 \le y \le 1$, $0 \le z \le 1$). (e,f) $0 \le x \le 1$, $0 \le y \le 1$, $-0.1 \le z \le 0.1$. (g,h) $0 \le x \le 1$, $0 \le y \le 1$, $0.4 \le z \le 0.6$. In panels (b) and (d), the grey spheres represent Ti atoms. In panels (c), (d), (e), and (f), the red, green, white, and orange arrows denote Li1–Li4, Li1′–Li4, Li2–Li4, and Li3–Li4 paths, respectively.

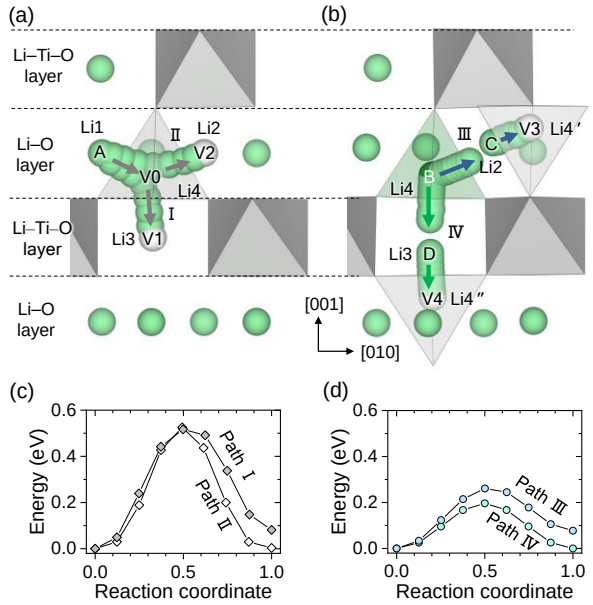

Figure 5. Li^+ ion migrations via (a,c) a vacancy mechanism and (b,d) an interstitialcy mechanism, which were investigated by DFT calculations and NEB method. (a) Li^+ ion migration paths I and II via the vacancy mechanism where a Li^+ ion A migrates from the Li1 site to vacant Li3 and Li2 sites, respectively, through a vacant Li4 interstitial site (Initial state of the migration along the path I: A at Li1 site, vacancy V0 at Li4 site, vacancy V1 at Li3 site; Final state of the migration along the path I: V0 at Li1 site, V1 at Li4 site, A at Li3 site; Initial state of the migration along the path II: A at Li1 site, V0 at Li4 site, V2 at Li2 site; Final state of the migration along the path II: V0 at Li1 site, V2 at Li4 site, A at Li2 site). (b) Li^+ ion migrations along paths III and IV via the interstitialcy mechanism where an interstitial Li^+ ion B pushes (kicks) another Li^+ ion at a lattice site (C for the path III; D for the path IV) out into an adjacent vacant interstitial site. In the path III, the B moves from Li4 to Li2 site and simultaneously another Li^+ ion C migrates from Li2 to vacant Li4′ site (Initial state: B at Li4 site, C at Li2 site, a vacancy V3 at Li4′ site; Final state: V3 at Li4 site, B at Li2 site, C at Li4′ site). In the path IV, a Li ion B moves from Li4 to Li3 site and simultaneously another Li ion D migrates from Li3 to vacant Li4″ site (Initial state: B at Li4 site, D at Li3 site, V4 at Li4″ site; Final state: V4 at Li4 site, B at Li3 site, D at Li4″ site). Energy barrier profiles along the paths I and II (c) and along the paths III and IV (d).

Conclusion

We have shown the existence of an interstitial Li4 atom at the tetrahedral site in the Li–O layer of β-Li_2TiO_3 using experimental and computational approaches. In the present work, we have successfully visualized the 3D network of Li-ion diffusion pathways, consisting of Li-ion diffusion pathways in the <001> and <110> directions of β-Li_2TiO_3. Here, for the first time, we propose an interstitialcy diffusion mechanism, in which a Li ion migrates through an interstitial site and lattice sites, for the series of Li-rich layered-oxide Li_2MO_3 (M = Ti, Mn, Sn, Ru, and/or Ir). We believe this new concept for the diffusion mechanism opens up new approaches in materials science, energy science, and solid state ionics researches on Li_2MO_3-based materials.

References

1. Chu, S.; Majumdar, A. Opportunities and challenges for a sustainable energy future. *Nature* **2012**, *488*, 294–303.
2. Aguesse, F.; López del Amo, J. M.; Roddatis, V.; Aguadero, A.; Kilner, J. A. Enhancement of the grain boundary conductivity in ceramic $Li_{0.34}La_{0.55}TiO_3$ electrolytes in a moisture-free processing environment. *Adv. Mater. Interfaces* **2014**, *1*, 1300143.
3. Takai, S.; Kamata, M.; Fujine, S.; Yoneda, K.; Kanda K.; Esaka. T. Diffusion coefficient measurement of lithium ion in sintered $Li_{1.33}Ti_{1.67}O_4$ by means of neutron radiography, *Solid State Ionics* **1999**, *123*, 165.
4. Thackeray, M. M.; Kang, S. H.; Johnson, C. S.; Vaughey, J. T.; Benedek, R.; Hackney, S. A. Li_2MnO_3-stabilized $LiMO_2$ (M = Mn, Ni, Co) electrodes for lithium-ion batteries. *J. Mater. Chem.* **2007**, *17*, 3112–3125.
5. He, P.; Yu, H.; Zhou, H. Layered lithium transition metal oxide cathodes towards high energy lithium-ion batteries. *J. Mater. Chem*. **2012**, *22*, 3680–3695.
6. Xu, B.; Qian, D.; Wang, Z.; Meng, Y. S. Recent progress in cathode materials research for advanced lithium ion batteries. *Mater. Sci. Eng. R Rep*. **2012**, *73,* 51–65.
7. Lu, J.; Peng, Q.; Wang, W.; Nan, C.; Li, L.; Li, Y. Nanoscale coating of $LiMO_2$ (M = Ni, Co, Mn) nanobelts with Li-ion-conductive Li_2TiO_3: Toward better rate capabilities for li-ion batteries. *J. Am. Chem. Soc.* **2013**, *135*, 1649–1652.
8. Zhao, E.; Liu, X.; Hu, Z.; Sun, L.; Xiao, X. Facile synthesis and enhanced electrochemical performances of Li_2TiO_3-coated lithium-rich layered $Li_{1.13}Ni_{0.30}Mn_{0.57}O_2$ cathode materials for lithium-ion batteries. *J. Power Sources* **2015**, *294*, 141–149.
9. Hu, G.; Zhang, M.; Wu, L.; Peng, Z.; Du, K.; Cao, Y. Enhanced Electrochemical Performance of $LiNi_{0.5}Co_{0.2}Mn_{0.3}O_2$ Cathodes Produced via Nanoscale Coating of Li^+-Conductive Li_2SnO_3. *Electrochim. Acta* **2016**, *213*, 547−556.
10. Pearce, P. E.; Perez, A. J.; Rousse, G.; Saubanère, M.; Batuk, D.; Foix, D.; McCalla, E.; Abakumov, A. M.; Van Tendeloo, G.; Doublet, M. L.; Tarascon, J. M. Evidence for anionic redox activity in a tridimensional-ordered Li-rich positive electrode β-Li_2IrO_3. *Nature mater*. **2017**, *16*, 580–586.
11. Sathiya, M.; Rousse, G.; Ramesha, K.; Laisa, C. P.; Vezin, H.; Sougrati, M. T.; Doublet M-L.; Foix, D.; Gonbeau, D.; Walker, W.; Prakash, A. S.; Ben Hassine, M.; Dupont, L.; Tarascon, J. M. Reversible anionic redox chemistry in high-capacity layered-oxide electrodes. *Nature mater*. **2013**, *12*, 827–835.
12. Sathiya, M.; Abakumov, A. M.; Foix, D.; Rousse, G.; Ramesha, K.; Saubanère, M.; Doublet, M. L.; Vezin, H.; Laisa, C. P.; Prakash, A. S.; Gonbeau, D. Origin of voltage decay in high-capacity layered oxide electrodes. *Nature mater.* **2015**, *14*, 230.
13. Raffray, A. R.; Akiba, M.; Chuyanov, V.; Giancarli, L.; Malang, S. Breeding blanket concepts for fusion and materials requirements. *J. Nucl. Mater.* **2002**, *307*, 21–30.
14. Konishi, S.; Enoeda, M.; Nakamichi, M.; Hoshino, T.; Ying, A.; Sharafat, S.; Smolentsev, S. Functional materials for breeding blankets—status and developments. *Nucl. Fusion* **2017**, *57*, 092014.
15. Knaster, J.; Moeslang, A.; Muroga, T. Materials research for fusion. *Nature Phys.* **2016**, *12*, 424–434.
16. Tanifuji, T.; Yamaki, D.; Nasu, S.; Noda, K. Tritium release behavior from neutron-irradiated Li_2TiO_3 single crystal. *J. Nucl. Mater.* **1998**, *258*, 543–548.
17. Ohno, H.; Konishi, S.; Nagasaki, T.; Kurasawa, T.; Katsuta, H.; Watanabe, H. Correlation behavior of lithium and tritium in some solid breeder materials. *J. Nucl. Mater.* **1985**, *133*, 181–185.
18. Yashima, M. Diffusion pathway of mobile ions and crystal structure of ionic and mixed conductors-A brief review. *J. Ceram. Soc. Japan* **2009**, *117*, 1055–1059.
19. Adams, S.; Rao, R. P. Structural requirements for fast lithium ion migration in $Li_{10}GeP_2S_{12}$. *J. Mater. Chem*. **2012**, *22*, 7687–7691.
20. Dorrian, J. F.; Newnham, R. E. Refinement of the structure of Li_2TiO_3. *Mater. Res. Bull.* **1969**, *4*, 179–183.

21. Kataoka, K.; Takahashi, Y.; Kijima, N.; Nagai, H.; Akimoto, J.; Idemoto, Y.; Ohshima, K. Crystal growth and structure refinement of monoclinic Li_2TiO_3. *Mater. Res. Bull.* **2009**, *44*, 168–172.
22. Laumann, A.; Fehr, K. T.; Boysen, H.; Hölzel, M.; Holzapfel, M. Temperature-dependent structural transformations of hydrothermally synthesized cubic Li_2TiO_3 studied by in-situ neutron diffraction. *Z. Kristallogr. Cryst. Mater.* **2011**, *226*, 53–61.
23. Vijayakumar, M.; Kerisit, S.; Yang, Z.; Graff, G. L.; Liu, J.; Sears, J. A.; Burton, S. D.; Rosso, K. M.; Hu, J. Combined 6, 7Li NMR and molecular dynamics study of Li diffusion in Li_2TiO_3. *J. Phys. Chem. C* **2009**, *113*, 20108–20116.
24. Shin, Y.; Ding, H.; Persson, K. A. Revealing the intrinsic Li mobility in the Li_2MnO_3 lithium-excess material. *Chem. Mater.* **2016**, *28*, 2081–2088.
25. Chen, Y.; Huo, M.; Song, L.; Sun, Z. Electrical and lithium ion dynamics in Li_2IrO_3 from density functional theory study. *RSC Adv.* **2014**, *4*, 42462–42466.
26. Monchak, M.; Dolotko, O.; Mühlbauer, M. J.; Baran, V.; Senyshyn, A.; Ehrenberg, H. Monoclinic β-Li_2TiO_3: neutron diffraction study and estimation of Li diffusion pathways. *Sol. St. Sci*. **2016**, *61*, 161–166.
27. Islam, M. M.; Bredow, T. Lithium Diffusion Pathways in β-Li_2TiO_3: A Theoretical Study. *J. Phys. Chem. C* **2016**, *120*, 7061–7066.
28. Gull, S. F.; Daniell, G. J. Image reconstruction from incomplete and noisy data. *Nature* **1978**, *272*, 686–690.
29. Collins, D. M. Electron density images from imperfect data by iterative entropy maximization. *Nature* **1982**, *298*, 49–51.
30. Nishimura, S.; Kobayashi, G.; Ohoyama, K.; Kanno, R.; Yashima, M.; Yamada, A. Experimental visualization of lithium diffusion in Li_xFePO_4. *Nature Mater.* **2008**, *7*, 707–711.
31. Yashima, M.; Itoh, M.; Inaguma, Y.; Morii, Y. Crystal structure and diffusion path in the fast lithium-ion conductor $La_{0.62}Li_{0.16}TiO_3$. *J. Am. Chem. Soc.* **2005**, *127*, 3491–3495.
32. Uno, W.; Fujii, K.; Niwa, E.; Torii, S.; Miao, P.; Kamiyama, T.; Yashima, M. Experimental visualization of oxide-ion diffusion paths in pyrochlore-type $Yb_2Ti_2O_7$. *J. Ceram. Soc. Japan* **2018**, *126*, 341–345.
33. Hoshino, T.; Kato, K.; Natori, Y.; Nakamura, M.; Sasaki, K.; Hayashi, K.; Terai, T.; Tatenuma, K. New synthesis method of advanced lithium titanate with Li_4TiO_4 additives for ITER-TBM. *Fusion Eng. Des.* **2009**, *84*, 956–959.
34. Ishigaki, T.; Hoshikawa, A.; Yonemura, M.; Morishima, T.; Kamiyama, T.; Oishi, R.; Aizawa, K.; Sakuma, T.; Tomota, Y.; Arai, M.; Hayashi, M. IBARAKI materials design diffractometer (iMATERIA)—Versatile neutron diffractometer at J-PARC. *Nucl. Instr. Meth. Phys. Res. A* **2009**, *600*, 189–191.
35. Oishi, R.; Yonemura, M.; Nishimaki, Y.; Torii, S.; Hoshikawa, A.; Ishigaki, T.; Morishima, T.; Mori, K.; Kamiyama, T. Rietveld analysis software for J-PARC. *Nucl. Instr. Meth. Phys. Res. A* **2009**, *600*, 94–96.
36. Ohoyama, K.; Kanouchi, T.; Nemoto, K.; Ohashi, M.; Kajitani, T.; Yamaguchi, Y. The new neutron powder diffractometer with a multi-detector system for high-efficiency and high-resolution measurements. *Jpn. J. Appl. Phys.* **1998**, *37*, 3319.
37. Yashima, M. In Situ Observations of Phase Transition Using High-Temperature Neutron and Synchrotron X-ray Powder Diffractometry. *J. Am. Cer. Soc.* **2002**, *85*, 2925–2930.
38. Izumi, F.; Momma, K. Three-dimensional visualization in powder diffraction. *Sol. St. Phenom*. **2007**, *130*, 15–20.
39. Izumi, F.; Dilanian, R. A. Recent Research Developments in Physics. *Part II* **2002**, *3*, 699–726.
40. Izumi, F.; Kumazawa, S.; Ikeda, T; Hu, W.-Z.; Yamamoto, A.; Oikawa, K.; *Mater. Sci. Forum* **2001**, *59*, 378–381.
41. Momma, K.; Izumi, F. VESTA 3 for three-dimensional visualization of crystal, volumetric and morphology data. *J. Appl. Cryst.* **2011**, *44*, 1272–1276.
42. Perdew, J. P.; Burke, K.; Ernzerhof, M. Generalized gradient approximation made simple. *Phys. Rev. Letters* **1996**, *77*, 3865–3868.
43. Blöchl, P. E. Projector augmented-wave method. *Phy. Rev. B* **1994**, *50*, 17953–17979.
44. Kresse, G.; Furthmüller, J. Efficient iterative schemes for ab initio total-energy calculations using a plane-wave basis set. *Phys. Rev. B* **1996**, *54*,

11169–11186.

45. Kresse, G.; Furthmüller, J. Efficiency of ab-initio total energy calculations for metals and semiconductors using a plane-wave basis set. *Comput. Mater. Sci.* **1996**, *6*, 15–50.

46. Henkelman, G.; Uberuaga, B. P.; Jónsson, H. A climbing image nudged elastic band method for finding saddle points and minimum energy paths. *J. chem. phys.* **2000**, *113*, 9901–9904.

47. Sale, M.; Avdeev, M. 3DBVSMAPPER: a program for automatically generating bond-valence sum landscapes. *J. Appl. Cryst.* **2012**, *45*, 1054–1056.

48. Brown, I. D.; Altermatt, D. Bond-valence parameters obtained from a systematic analysis of the inorganic crystal structure database. *Acta Crystallogr., Sect. B: Struct. Sci*. **1985**, *41*, 244−247.

49. Tang, W.; Sanville, E.; Henkelman, G. A grid-based Bader analysis algorithm without lattice bias. *J. Phys.: Condens. Matter* **2009**, *21*, 084204.

50. Murphy, S. T.; Hine, N. D. Point defects and non-stoichiometry in Li_2TiO_3. *Chem. Mater*. **2014**, *26*, 1629–1638.

51. Hoshino, T.; Tanaka, K.; Makita, J.; Hashimoto, T. Investigation of phase transition in Li_2TiO_3 by high temperature X-ray diffraction. *J. Nucl. Mater.* **2007**, *367*, 1052–1056.

52. Roux, N. in: Noda, K. (ed.), *Proceedings Sixth International Workshop on Ceramic Breeder-Blanket Interactions* (No. JAERI-CONF--98-006), **1998**, 139–147.

53. Shi, S.; Lu, P.; Liu, Z.; Qi, Y.; Hector Jr, L.G.; Li, H.; Harris, S. J. Direct calculation of Li-ion transport in the solid electrolyte interphase. *J. Am. Chem. Soc*. **2012**, *134*, 15476–15487.

ASSOCIATED CONTENT

Supporting Information

The supporting information is available free of charge on the ACS Publications website at DOI; 10.1021/acsaem.9b00639.

Refined crystal structures, MEM nuclear-density distributions, Rietveld patterns of the neutron diffraction data measured with the HERMES diffractometer, refined crystallographic parameters, local configuration optimized by DFT calculations, thermogravimetric data, reined lattice parameters and BVS, occupancy factors obtained by Rietveld analysis and MEM, BVS map, migration energy barriers by NEB calculations, and effective charge by Bader analysis. The Supplementary Information is available free of charge on the ACS Publications website at DOI:

Figure S1–S12 and Table S1–7 in SI.docx.

AUTHOR INFORMATION

Corresponding authors

*Email k-mukai@iae.kyoto-u.ac.jp (K.M.)

*Email yashima@cms.titech.ac.jp (M.Y.)

ORCID

Keisuke Mukai: 0000-0001-8067-8732

Masatomo Yashima: 0000-0001-5406-9183

Keisuke Hibino: 0000-0002-0587-3287

Notes The authors declare no competing financial interest.

Notes

The authors declare no competing financial interest.

ACKNOWLEDGEMENTS

The neutron diffraction measurements performed with the approval 22K369(HERMES) and 2010A0008 (iMATERIA).). The authors would like to thank Prof. K. Sasaki, Dr. K. Omoto, Prof. T. Ishigaki, and Prof. A. Hoshikawa for assistance in the neutron diffraction experiments. K.M. was supported by a JSPS Research Fellowship DC2 (24-5331). M.Y. acknowledges the support by a Grant-in-Aid for Scientific Research (KAKENHI, Nos. JP15H02291, JP16H06441, JP17H06222) from the Ministry of Education, Culture, Sports, Science and Technology of Japan, and by JSPS Core-to-Core Program, A. Advanced Research Networks (Solid Oxide Interfaces for Faster Ion Transport).